Volume 2
Number 6
November 2025
Pages 1495–1930

RSC Applied Interfaces

rsc.li/RSCApplInter

ISSN 2755-3701

ROYAL SOCIETY OF CHEMISTRY

PAPER
Leila F. Deravi *et al.*
Enhanced colour modulation in printed electrochromic pixels *via* optimization of a polymer gel electrolyte

RSC Applied Interfaces

ROYAL SOCIETY OF CHEMISTRY

PAPER

View Article Online
View Journal | View Issue

Cite this: *RSC Appl. Interfaces*, 2025, **2**, 1591

Enhanced colour modulation in printed electrochromic pixels *via* optimization of a polymer gel electrolyte

Taehwan Kim,[a] Patrick A. Sullivan,[a] Jack Twiddy,[b] Kaila Peterson,[c] Lasanthi Sumathirathne,[a] Kirstie M. K. Queener,[b] Michael Daniele[bc] and Leila F. Deravi*[a]

Received 21st June 2025,
Accepted 25th August 2025

DOI: 10.1039/d5lf00176e

rsc.li/RSCApplInter

With the growing demand for thinner and more flexible electrochromic devices (ECDs), proper electrolyte selection is critical for the design and implementation of these systems. Compared to a traditional liquid electrolyte, polymer gel electrolytes have received growing application in ECDs due to their efficient ion transport, high stability, and, most importantly, zero risk of leakage during device integration. In this work, we capitalize on these features in the design, fabrication, and testing of a flexible and multifunctional polymer gel electrolyte using a polyvinylidene fluoride-*co*-hexafluoropropylene (PVDF-HFP) matrix enriched with ionic liquids and plasticizers that interface with adjacent electrochromic pixels. This polymer gel electrolyte remains stable at room temperature, enabling operation of ECD pixel elements over 2750 cycles and 2.5 days of continuous operation. Applications such as passive color filtering using the electrolyte are also explored, highlighting its potential to improve operation and expand colour range without modification of the electrochromic film.

Introduction

Traditional electrochromic devices (ECDs) are assembled with up to five layers, including two transparent conductive electrodes, two electrochromic functional layers, and a central electrolyte, all contained in a sealed package. Such features make these devices technically challenging to customize, scale, control, and integrate within a display as an array of pixels.[1] While there have been significant advancements in fabricating electrochromic pixels for diverse use cases *via* patterning,[2,3] multi-material blending,[4,5] colour filtering,[6] or inclusion of nanomaterials,[7,8] the form and function of the electrolytes used in these applications are highly variable. Of the common electrolyte forms (*i.e.* liquid,[9–11] solid,[12–14] or gel[15–17]), gel electrolytes offer an excellent balance of flexibility, ionic conductivity, and stability. Specifically, polymer gel-based electrolytes (PGE) like polyethylene glycol (PEG),[18,19] polyvinyl alcohol (PVA),[20–22] and polyethylene oxide (PEO),[23,24] combined with a salt such as lithium perchlorate or lithium hexafluorophosphate, have seen some success when integrated within ECDs; however, limited mechanical and storage stability are common challenges with PVA- or PEO-based gels, primarily due to their high moisture sensitivity.[25,26] Because of this, the gels are also susceptible to chemical changes over time, which can alter their ionic conductivity, electrochemical performance, and mechanical properties. This instability can lead to ionic salt leakage, which compromises ECD performance and longevity. As such, there is an ongoing effort to explore new combinations of polymer matrices and additives that can enhance the performance of these electrolytes to improve their durability in a way that is generalizable to multiple ECD configurations.

Polyvinylidene fluoride-*co*-hexafluoropropylene (PVDF-HFP)[27–29] has emerged as a promising alternative to PEG, PVA, and PEO within PGEs. Unlike PVA- or PEO-based electrolytes, PVDF-HFP is more resistant to chemical modification during the charge/discharge cycles typically experienced by ECDs. In addition to its electrochemical stability, PVDF-HFP is well known for its high tensile strength and durability.[30] PVDF-HFP has low moisture sensitivity compared to PVA and PEO and is less susceptible to the swelling or plasticization effects that may compromise the performance of other gel-based electrolytes.[31] However, notable drawbacks of PVDF-HFP include its dependence on organic solvents and higher melting temperatures during processing, as well as its poor degradability, brittle mechanical properties, and low ionic conductivity when cast

[a] *Department of Chemistry and Chemical Biology, Northeastern University, Boston, MA 02115, USA. E-mail: l.deravi@northeastern.edu*
[b] *Joint Department of Biomedical Engineering, University of North Carolina at Chapel Hill and North Carolina State University, Chapel Hill, North Carolina 27599, USA*
[c] *Department of Electrical and Computer Engineering, North Carolina University, Raleigh, North Carolina 27606, USA*

as films.[32,33] While the environmental footprint of PVDF-HFP films remains a challenge, their mechanical and ion-transport properties can be addressed by carefully optimizing plasticizers and salt content.

Recognizing this potential, we developed a PGE based on PVDF-HFP and systematically evaluated its performance within printed electrochromic pixels. We examined the ionic conductivity and process versatility of the PGE in combination with selected additives and plasticizers, which were integrated to enhance the electrolyte's functional performance and practical applicability within ECD systems. Pixels were fabricated using inkjet printing of cephalopod-derived pigment xanthommatin (Xa) and conductive poly(3,4-ethylenedioxythiophene) polystyrene sulfonate (PEDOT:PSS) inks, previously demonstrated to achieve red (reduced) and yellow (oxidized) states when paired with liquid electrolytes.[34,35] Building on foundational work by Dzulkipli *et al.*,[36] we optimized their PGE formulation, highlighting key modifications that significantly improved electrolyte performance. Furthermore, we evaluated the effectiveness of this optimized electrolyte in novel configurations of inkjet-printed electrochromic pixels.

Experimental

Polymer gel electrolyte (PGE) and characterization

PGE fabrication. The principal component of the PGE was a 0.2 g mL^{-1} solution of poly(vinylidene fluoride-*co*-hexafluoropropylene) (PVDF-HFP, Sigma-Aldrich, M_w = 400 000) dissolved in acetone. The PVDF-HFP solution was doped with various combinations and v/v ratios of propylene carbonate (PC, Sigma Aldrich), 1-butyl-3-methylimidazolium tetrafluoroborate (IL, Sigma-Aldrich), and hydroquinone (HQ, Acros Organics).[34,35] To optimize PGE performance, the components of the LEL were varied according to the values listed in Table 1, prior to combination with PVDF-HFP to achieve final v/v ratios of 7 : 7, 7 : 5, and 7 : 3 PVDF-HFP : LEL dopant. After mixing, the solutions were vortexed for 1 min and sonicated to remove bubbles. The solutions were then placed in a vacuum chamber for 10 min to degas the mixtures equipped with a vacuum pump (MaximaDry, Fisher Scientific), achieving a maximum pressure of approximately 15 psig prior to casting as film. Next, 3 mL of each combined mixture was drop-cast onto a pre-cleaned glass slide, then evenly spread into a film using a doctor blade with a 1 mm gap from the substrate. The PGE was sealed and stored at room temperature in the dark to prevent exposure to air until further use.

Table 1 LEL dopant combinations added to 0.2 g mL^{-1} PVDF-HFP solution. The italicized row (containing all three dopants) was used in the variable ratio experiments (7 : 7, 7 : 5, and 7 : 3 PVDF-HFP : LEL dopant) shown in Fig. 1

Sample name	PC (g)	IL (g)	HQ (g)
PC	3.600	—	—
PC + HQ	3.600	—	0.003
PC + IL	2.000	1.600	—
IL	—	3.600	—
IL + HQ	—	3.600	0.003
PC + IL + HQ	*2.000*	*1.600*	*0.003*

Mechanical testing of the PGE formulations

Young's modulus was calculated for various PGE formulations using stress–strain curves obtained with a custom-built uniaxial tensile tester. The system consisted of a high-resolution linear actuator (M-230, Physik Instrumente) and a stepper motor-controlled load cell (Model 31, Honeywell). Force measurements were recorded and controlled using the MTESTQuattro controller (ADMET). The specimens were cut into rectangular shapes, 1 mm wide and 21 mm long. The thickness of each sample was measured with precision calipers (Starrett), and tests were conducted at a constant rate of 0.1 mm s^{-1} until failure or until the uniaxial tester reached its maximum strain. Mechanical testing was carried out with three replicates (n = 3) for each experimental condition, and standard deviations were calculated to quantify variability.

Transmission spectra of the PGE formulations

Transmission characterization of the PGE formulations was carried out with a spectrophotometer (Flame-S-vis-NIR, Ocean Optics) in transmission mode between 400 and 800 nm. The PGE was positioned between the two optical fibers, and transmission spectra were recorded.

Electrochromic pixel fabrication and assembly

Ink formulation. 200 μL of xanthommatin (Xa)[34,35] (2 mg mL^{-1} in 0.05 M 2-(*N*-morpholino) ethane sulfonic acid buffer) was combined with 1.6 mL PEDOT:PSS ink (PEDOT-Jet 40, PEDOTinks). The resulting formulation was filtered using a 1 μm polytetrafluoroethylene syringe prior to loading into the ink chamber of a Samba printhead cartridge (Dimatix, Fujifilm).

Substrate preparation

ITO-coated PET sheets (Sigma Aldrich, surface resistivity = 60 Ω sq^{-1}) were masked and etched using zinc powder as described previously.[37] Briefly, adhesive vinyl masks were produced using a drag knife vinyl cutter (Maker 3, Cricut) and placed upon ITO-coated PET sheets. An excess of zinc powder (Fisher Scientific, mean particle size of 7.5 μm) was distributed onto the masked ITO substrate to completely cover the area, which was then soaked in 3 M HCl for 10 s to etch and remove the ITO from the unmasked region. After the etching was complete, substrates were rinsed immediately with DI water, and Kimwipes were used to remove any remaining zinc. After the masks were removed, the substrate was visually inspected for flaws, and any remaining residue was similarly cleared. Prior to printing,

etched ITO sheets were additionally cleaned using UV-ozone (Model 30, Jelight) for 30 min.

Electrochromic pixel printing and device assembly

Electrochromic pixels were fabricated as two 1 by 1 cm squares separated by a 0.1 cm gap, with each square featuring 0.1 by 0.3 cm "tail" for interfacing with an external power supply. The pixels were printed onto the surface of the etched ITO substrate using a piezoelectric inkjet printer (Diamtix Materials Printer DP-285, Fujifilm) at room temperature. Printing was performed using a Samba print cartridge, with each pixel composed of 10 printed layers. Prior to all print cycles, we would manually inspect the nozzles for consistent drop formation. From here, we consistently employed between 1 and 5 nozzles (out of the 12 available nozzles) at a jetting frequency of 33 kHz and a driving voltage of 39 V to fabricate the electrochromic pixels. Following printing, the electrodes were annealed at 50 °C overnight and then left at room temperature for 1 h prior to testing. Prepared PGE sheets were cut into 2.1 by 1 cm sections and manually aligned over the printed electrodes to complete each pixel.

Device characterization

Electrochemical characterization. Pixels were characterized using a potentiostat (Interface 1000B, Gamry). Electrochemical impedance spectroscopy (EIS) was conducted from 10^4 Hz to 10^{-1} Hz at an amplitude of 20 mV using test cells made from two planar stainless-steel electrodes, which together formed a symmetrical cell.

Optical contrast, switching, and stability. Reflectance measurements were collected at 45° relative to the pixel surface using a spectrophotometer (Flame-S-vis-NIR, Ocean Optics). Spectra were collected every 10 s during application of a forward or reverse bias potential. The change in optical density (ΔOD) was measured using eqn (1) at 555 nm, similar to previous reports.[34,35] Briefly, the % reflectance at 555 nm obtained over 5 cycles was used to determine R_{ox} and R_{red} corresponding to positive and negative polarity, respectively, and ΔOD was then calculated.

$$\Delta OD = \log R_{ox}/R_{red} \quad (1)$$

Colour efficiency (CE) was calculated using eqn (2).[38] Here, ΔOD was determined from eqn (1) and Q (the transferred charge) was calculated from the integrated current collected using chronoamperometry.

$$CE = \Delta OD/Q \quad (2)$$

Colour analysis

An iPhone 8 plus (12-megapixel resolution camera, 60 frames per s) was used to collect videos of the pixels during polarization. These videos were processed with VideoProc Converter (Digiarty) to extract 1 frame per 2 s of video. Images were then analysed with ImageJ using the RGB Measure plugin.[39] Measured reflectance spectra were converted to the International Commission on Illumination (CIE) *xyY* color space using a MATLAB script.[40] When analysing differences in presented colours, ΔE was calculated using eqn (3),[41] where L^*, a^* and b^* refer to the coordinates in the CIELAB colour space. Here, the subscript notation 1 denotes the oxidized state, and 2 denotes the reduced state of the pixel.

$$\Delta E = \sqrt{(L_2^* - L_1^*)^2 + (a_2^* - a_1^*)^2 + (b_2^* - b_1^*)^2} \quad (3)$$

Statistical analysis

Statistically significant differences in electrochemical and mechanical properties of the PGE samples prepared with varying PVDF-HFP : LEL ratios (n = 3) was assessed using a two-tailed t-test. A p-value threshold of 0.05 ($p < 0.05$) was used to define statistical differences between conditions. Calculations were performed in Microsoft Excel using the *T*.TEST function (two-tailed, two-sample assuming equal variances).

Results and discussion

We first investigated how individual components of our previous liquid electrolyte (LEL) formulation (PC, HQ, and IL)[35] influenced the performance of a PGE made from PVDF-HFP. To understand this relationship, we systematically evaluated each component (and combinations thereof) in the polymer matrix according to Table 1 and characterized the resulting electrochemical properties of the electrolyte. EIS was used to collect impedance data for all electrolyte permutations. These data were fit to a Randles equivalent circuit containing a Warburg element (W) and constant phase element (CPE), representing the electrolyte double layer capacitance. The parameters R_s and R_{ct} were used to represent the electrolyte resistance and charge-transfer resistance, respectively. Since the circuit contains two R_{ct} elements, their average value was calculated and presented (Fig. 1A).[42] In general, each electrolyte additive contributed to lower resistances relative to the control PVDF-HFP without LEL, which presented an electrolyte resistance of $1.3 \times 10^3 \pm 0.7 \times 10^3$ Ω and a charge transfer resistance of $402.6 \times 10^3 \pm 193.3 \times 10^3$ Ω (Fig. S1 and Table S1). While PC improved the initial brittleness of the PVDF-HFP matrix (Fig. S2), the presence of all three additives (IL, PC, and HQ) contributed to reduced electrolyte and charge transfer resistances relative to the control (Table S1). This observation is in agreement with past works, which presented select combinations of IL, PC, and HQ in electrolytes to enhance ionic conductivity,[43] facilitate ionic diffusion,[44] and participate as a redox mediator,[45,46] respectively. Without each of these specific additives, the electrolyte could not sufficiently support the polarization changes required for colour change of our electrochromic pixels (Fig. S3).

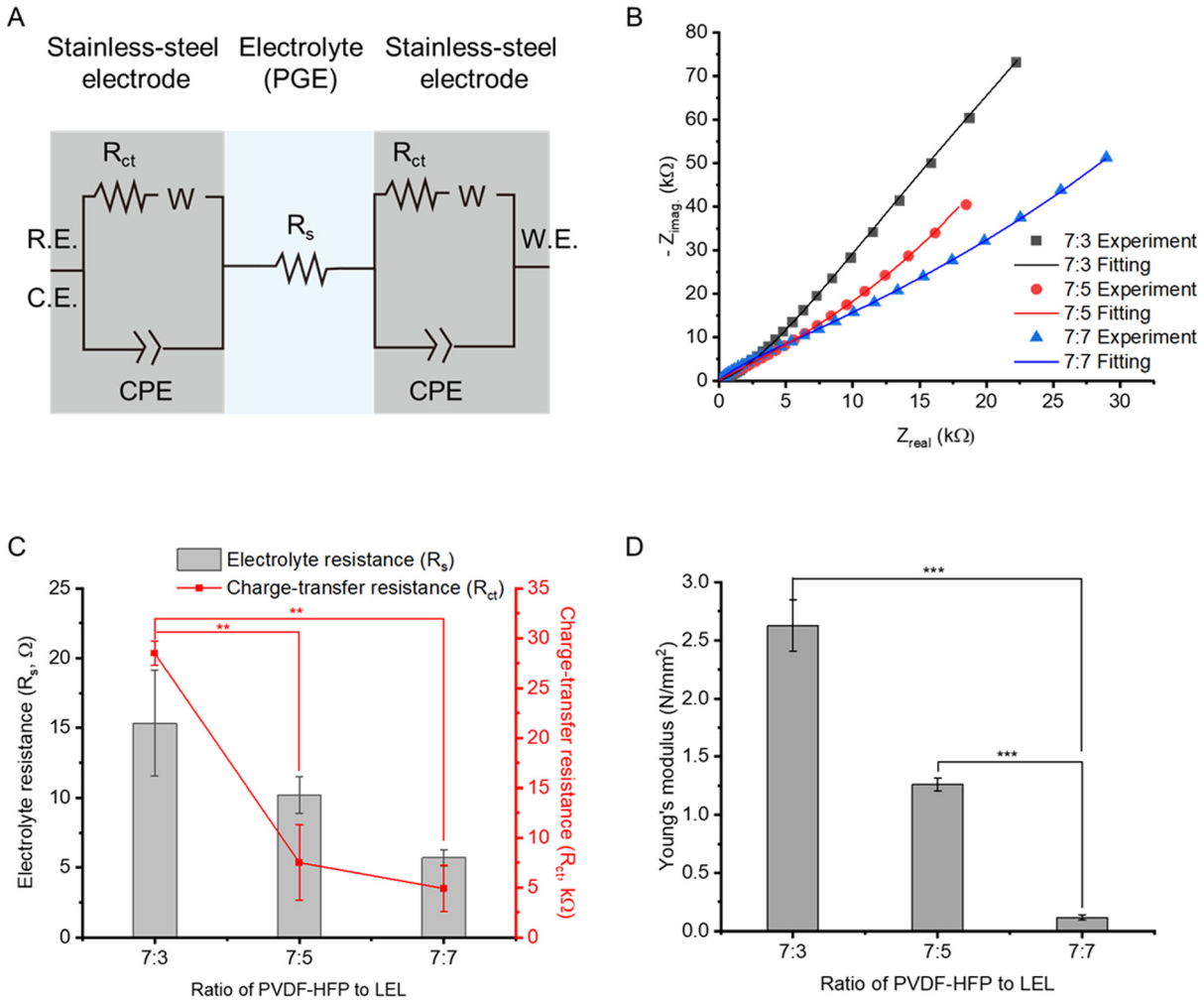

Fig. 1 Optimization of the PGE. (A) Schematic representation of the modified circuit model, in which the electrolyte resistance (R_s) and charge-transfer resistance (R_{ct}) were extracted by fitting the experimental EIS data. (B) Experimental EIS data overlaid against simulated results from the modified circuit for the PGE, fit from data collected in each condition (representative data shown for n = 1). (C) Changes in the v/v ratios of PVDF-HFP to LEL affect the electrolyte and charge transfer resistance as measured by EIS. Statistically significant differences in R_{ct} values ($p < 0.01$) are indicated by asterisks. (D) Varying the v/v ratios influences the Young's modulus of the PGE. Statistically significant differences in Young's modulus ($p < 0.001$) are indicated by asterisks. n = 3, mean ± standard deviation.

Based on these data, we selected the LEL dopant combination that provided the lowest resistance (including PC, IL, and HQ), and combined it with PVDF-HFP at v/v ratios of 7 : 7, 7 : 5, and 7 : 3 (PVDF-HFP : LEL) to make a PGE. Higher LEL values reduced the electrolyte resistance of the PGE from 15.4 ± 4.8 Ω (7 : 3) to 10.2 ± 1.3 Ω (7 : 5) and 5.7 ± 0.6 Ω (7 : 7) (Fig. 1B). This trend was also observed for measured charge transfer resistances which decreased from $28.5 \times 10^3 \pm 1.2 \times 10^3$ Ω (7 : 3) to $7.5 \times 10^3 \pm 3.8 \times 10^3$ Ω (7 : 5) and $4.9 \times 10^3 \pm 2.3 \times 10^3$ Ω (7 : 7) (Fig. 1B and C). Beyond these measured electrical changes, we observed significant variations in the Young's modulus of the materials from 2.63 ± 0.22 N mm^{-2} (7 : 3) to 0.12 ± 0.02 N mm^{-2} (7 : 7) (Fig. 1D). No significant variation was observed when compared to the 7 : 5 composition. These values were significantly smaller than the control PVDF-HFP film (no LEL), which had a Young's modulus of 160.8 ± 10.2 N mm^{-2}, further supporting that the inclusion of the LEL is necessary to decrease the stiffness of the original PVDF-HFP film. To understand how the presence of the LEL impacted the optical clarity of the electrolyte, we measured light transmission through the films. The 7 : 3, 7 : 5, and 7 : 7 v/v PVDF-HFP : LEL dopant samples transmitted 66.0 ± 2.4, 82.5 ± 1.6, and 79.9 ± 2.8% of incident light at 555 nm, respectively, compared to 28.4 ± 11.4% PVDF-HFP only (Fig. S4). When taken together, the addition of the LEL components appeared to increase the overall free volume and polymer chain mobility within the original, semi-crystalline PVDF-HFP matrix,[47] leading to decreased resistance with increased flexibility and transparency. Across all the metrics tested, the 7 : 5 ratio emerged as the condition with the best overall balance of low resistance, high transparency, and improved mechanical flexibility relative to the PVDF-HFP-only control (Table S1). Thus, we selected this ratio for all subsequent experiments.

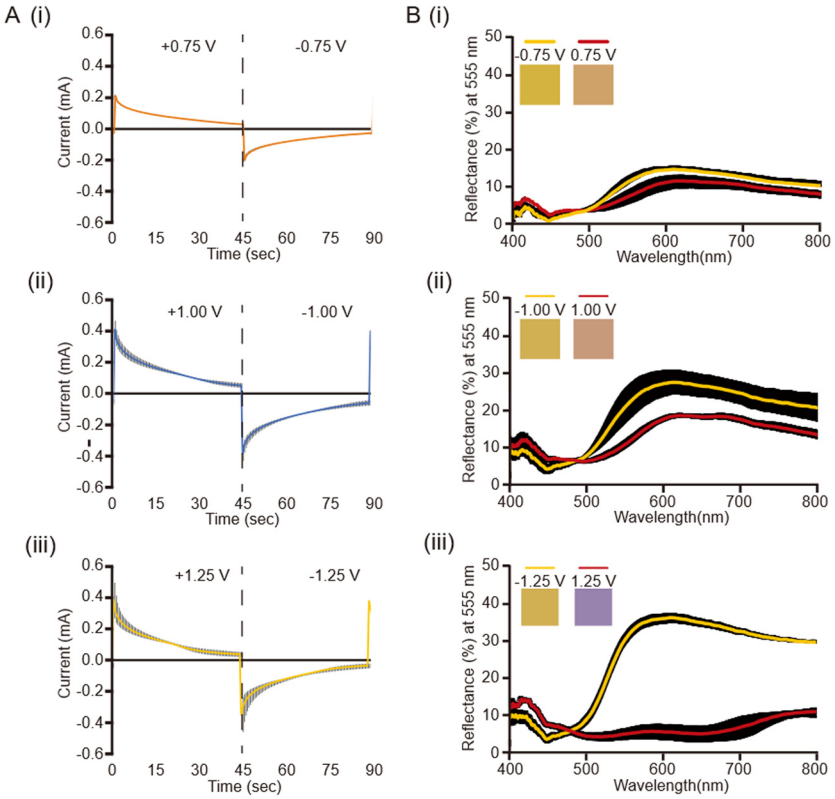

Fig. 2 Comparison of (A) chronoamperometry data for pixels using the 7 : 5 v/v ratio PGE under applied voltages of: (i) ±0.75, (ii) ±1.00, and (iii) ±1.25 V. (B) Reflectance spectra of the pixels with the measured electrode in its reduced (reverse-polarized) and oxidized (forward-polarized) states, measured after 45 s of the following applied potentials: (i) ±0.75, (ii) ±1.00, and (iii) ±1.25 V. Square insets depict the colours corresponding to the obtained reflectance spectra. n = 3, mean ± standard deviation (represented by black shading around the lines).

We next tested how different driving voltages affected pixel performance. We observed an increase in current (Fig. 2A) and colour saturation (Fig. 2B) at applied potentials above ±1 V. Colour efficiency (CE) increased from 45.5 ± 8.2, 45.5 ± 4.3, and 98.8 ± 17.5 cm^2/C for the ±0.75, ±1, and ±1.25 V conditions, respectively (Table S2). Despite the higher colour efficiencies observed at ±1.25 V, we only observed the yellow/red colours specific to the cephalopod pigment Xa at potentials less than ±1 V. At or above this threshold, the blue colours associated with the PEDOT:PSS redox transition dominated the observed pixel colour. As a result, we maintained the applied potential of ±0.75 V to maximize the yellow/red colour space in our experiments.

Finally, we evaluated the long-term stability of the PGE by continuously powering the pixels for 2750 cycles (~69 h) while measuring pixel current and colour change (Fig. S5). We observed a 31.0 ± 0.3% reduction in peak current at 0.75 V and a 28.5 ± 0.9% reduction in peak current at −0.75 V calculated from the averages of the first five and final five cycles, respectively. Despite this reduction in peak current, a negligible increase in reflectance at 555 nm was observed for both polarization directions (0.4 ± 0.2% and 1.7 ± 0.2% for the oxidized and reduced states, respectively) over 2750 cycles (Fig. S5). This observation suggests that changes in pixel impedance during prolonged use did not adversely impact pixel functionality. Although the magnitude of the current is directly related to the redox reactions responsible for colour change (as it corresponds to the total charge transferred into the cell), it is possible that pixels undergo a conditioning process or maturation phase that facilitates more efficient charge transfer with repeated cycling. Voltage also plays a critical role, as sufficient overpotential is necessary to drive these electrochromic reactions.

To explore applications of these pixels, we applied the PGE across a 2 × 2-pixel array integrated with a custom printed circuit board (Fig. 3A). Here, one pixel is represented by the adjacent blocks, which function as both the display element and the counter/reference electrodes. These pixels were controlled with off-board electronics which applied ±0.75 V to enable synchronized colour changes across the display. Our results demonstrated reproducible and visually uniform colour switching across the pixel array (Fig. 3B).

Given the ease of fabrication and use of the PGE, we explored how passive elements embedded within the matrix, such as organic dyes, could impact pixel performance. To test this, we selected indigo carmine and Congo red as dopants, given their distinct blue and red hues, respectively, and incorporated them at a 0.6 wt% within the PGE to produce optical filters that were layered on top of our printed pixels (Fig. 4A). The presence of the dye-doped electrolytes activated

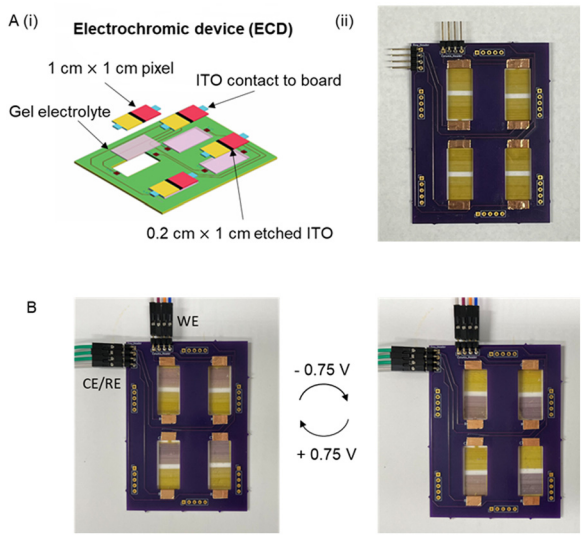

Fig. 3 Integration of the PGE with arrayed pixels. (A)(i) Schematic of the board and pixel integration scheme and (ii) image showing the integrated pixels (each consisting of two 1 cm^2 printed squares) with the PGE on the printed circuit board before polarization. (B) Chronoamperometric application of a ±0.75 V DC potential (200 s per cycle) demonstrated the capability for synchronized colour change. Within the pixel array.

with ±0.75 V across multiple pixels demonstrated notable changes in the visible colours relative to the control electrolyte containing no dye (Fig. 4B(i) and (ii) and C(i)). A further comparison at a higher applied voltage ±1.5 V is shown in Fig. 4B(iii) and (iv) and (C)(ii). These colour variations were analysed using the CIE 1931 colour space,[48] highlighting distinguishable changes to the colour output of the pixels with and without dye-doped electrolyte (Fig. S6). These differences were further characterized by a dimensionless parameter, ΔE, which expresses colour difference as a single numerical value.[41] For our pixels, we calculated a ΔE of 25.53, 12.58, and 10.64 at an applied voltage of ±0.75 V and 27.11, 30.21, and 35.2 at an applied voltage of ±1.5 V after forward and reverse polarization using the transparent PGE, the indigo carmine-loaded PGE, and the Congo red-loaded PGE, respectively. At higher voltages, the colour transition became more vivid, and the overall intensity increased significantly. However, at this elevated voltage, the optical appearance was largely influenced by the dopant PEDOT:PSS, which masked the contribution of Xa. Because all ΔE values exceeded 10, all pixels could be classified as clearly distinguishable.

Conclusions

In this study, we overcame the limitations of our previous pixel design by developing a new integrated system that replaces the LEL with a PGE. This enhancement, along with the use of conductive ITO-coated PET substrates and key additives like PC, IL, and HQ, led to significant improvements in electrochemical performance, speed, and scalability. The inclusion of PC

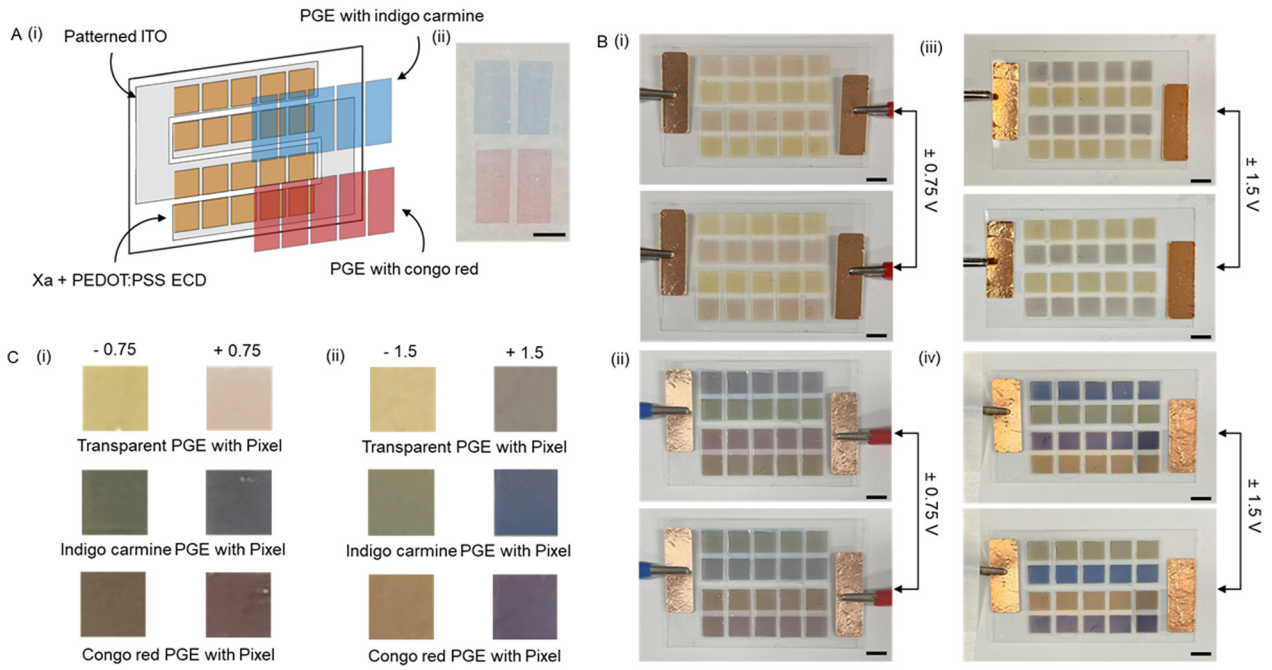

Fig. 4 Using the PGE layer as a colour filter across multiple electrochromic pixels. (A)(i) Schematic illustration of multipixel array and (ii) optical images of PGEs containing indigo carmine (blue) and Congo red (red). Scale bar = 1 cm. (B) Images of colour switching using the (i and iii) transparent PGE and (ii and iv) dye-doped PGE, upon application of ±0.75 and ±1.5 V. Scale bar = 1 cm. (C)(i) Comparison of colour states before and after activation with and without organic dye-doped PGEs at applied voltage of ±0.75 V, and (ii) colour states before and after activation with and without organic dye-doped PGEs at applied voltage of ±1.5 V.

contributed to the flexibility of the electrolyte by plasticizing the inherently rigid PVDF-HFP matrix, while IL enhanced ionic conductivity, reducing electrolyte resistance, and HQ reduced charge-transfer resistance through its reversible redox reactions. Additionally, optimizing the PVDF-HFP : LEL ratio resulted in notable improvements (particularly in the 7 : 5 ratio) in both electrolyte and charge transfer resistances, as well as in mechanical and light transmission properties. Long-term stability testing showed stable PGE performance over 2750 cycles, with stable pixel performance. Additionally, we successfully demonstrated alternative applications of the PGE as a passive colour filter to generate additional colours in our pixels. Future work will focus on scaling and miniaturizing the pixel array with appropriate integrated electronics, while further enhancing the pixel chemistry to enable more dynamic electrochromic display systems.

Author contributions

T. K. and P. A. S. designed the experiments, including fabrication, measurement, and data analysis. J. T., K. P., K. Q., and M. D. contributed to the design and testing of the electronic circuit board; J. T. also contributed to EIS analysis. J. T., K. P., K. Q. and M. D. contributed to the manuscript. L. S. formulated the initial PGE. L. F. D. and M. D. led the investigation and supervised the project. T. K., P. A. S., and L. F. D. prepared the manuscript.

Conflicts of interest

The authors declare no competing financial interests.

Data availability

Supplementary information is available. See DOI: **https://doi.org/10.1039/D5LF00176E**.

The data supporting this article have been included as part of the SI.

Acknowledgements

This work was supported by the Office of Naval Research (Award N00014-22-1-2053).

References

1 C. Gu, A.-B. Jia, Y.-M. Zhang and S. X.-A. Zhang, *Chem. Rev.*, 2022, **122**, 14679–14721.
2 J. W. Kim and J. M. Myoung, *Adv. Funct. Mater.*, 2019, **29**, 1808911.
3 R. Brooke, J. Edberg, X. Crispin, M. Berggren, I. Engquist and M. P. Jonsson, *Polymer*, 2019, **11**, 267.
4 R. H. Bulloch, J. A. Kerszulis, A. L. Dyer and J. R. Reynolds, *ACS Appl. Mater. Interfaces*, 2015, **7**, 1406–1412.
5 M. Li, O. A. Yassin, M. L. Baczkowski, X. Zhang, R. Daniels, A. A. Deshmukh, Y. Zhu, M. T. Otley and G. A. Sotzing, *Org. Electron.*, 2020, **84**, 105748.
6 I. J. Ko, J. H. Park, G. W. Kim, R. Lampande and J. H. Kwon, *J. Inf. Disp.*, 2019, **20**, 155–160.
7 L. Shao, X. Zhuo and J. Wang, *Adv. Mater.*, 2018, **30**, 1704338.
8 Y. Liu, L. Huang, S. Cao, J. Chen, B. Zou and H. Li, *Nanophotonics*, 2024, **13**, 155–172.
9 A. Brazier, G. Appetecchi, S. Passerini, A. S. Vuk, B. Orel, F. Donsanti and F. Decker, *Electrochim. Acta*, 2007, **52**, 4792–4797.
10 H. Moulki, D. H. Park, B.-K. Min, H. Kwon, S.-J. Hwang, J.-H. Choy, T. Toupance, G. Campet and A. Rougier, *Electrochim. Acta*, 2012, **74**, 46–52.
11 D. Zhou, R. Zhou, C. Chen, W.-A. Yee, J. Kong, G. Ding and X. Lu, *J. Phys. Chem. B*, 2013, **117**, 7783–7789.
12 S. J. Yoo, J. W. Lim and Y.-E. Sung, *Sol. Energy Mater. Sol. Cells*, 2006, **90**, 477–484.
13 W. Li, X. Zhang, X. Chen, Y. Zhao, L. Wang, M. Chen, J. Zhao, Y. Li and Y. Zhang, *Chem. Eng. J.*, 2020, **398**, 125628.
14 X. Chen, S. Dou, W. Li, D. Liu, Y. Zhang, Y. Zhao, Y. Li, J. Zhao and X. Zhang, *Chem. Commun.*, 2020, **56**, 5018–5021.
15 S. Santiago, M. Aller, F. J. del Campo and G. Guirado, *Electroanalysis*, 2019, **31**, 1664–1671.
16 W. C. Poh, A. L. S. Eh, W. Wu, X. Guo and P. S. Lee, *Adv. Mater.*, 2022, **34**, 2206952.
17 B. Ma, L. Tang, Y. Zhang, Z. Li, J. Zhang and S. Zhang, *ACS Appl. Mater. Interfaces*, 2024, **16**, 48927–48936.
18 C. Y. Jeong, T. Kubota, C. Chotsuwan, V. Wungpornpaiboon and K. Tajima, *J. Electroanal. Chem.*, 2021, **897**, 115614.
19 G. Xing, L. Wu, G. Kuang, T. Ma, Z. Chen, Y. Tao, Y. Kang and S. Zhang, *Electrochim. Acta*, 2022, **432**, 141216.
20 S. Vijayaraghavan, N. Raj and N. K. AK, *Electrochim. Acta*, 2024, **504**, 144948.
21 S. Zhao, W. Huang, Z. Guan, B. Jin and D. Xiao, *Electrochim. Acta*, 2019, **298**, 533–540.
22 J. O. Dennis, M. Shukur, O. A. Aldaghri, K. H. Ibnaouf, A. A. Adam, F. Usman, Y. M. Hassan, A. Alsadig, W. L. Danbature and B. A. Abdulkadir, *Molecules*, 2023, **28**, 1781.
23 I. Sorar, G. Atak, I. B. Pehlivan, C. G. Granqvist and G. A. Niklasson, *Solid State Sci.*, 2023, **137**, 107127.
24 G. Liu, Z. Wang, J. Wang, H. Liu and Z. Li, *J. Colloid Interface Sci.*, 2024, **655**, 493–507.
25 S. Na, J. Yeom, Y. Chang, Y. Kwon, C. Park, Y.-E. Shin, Y.-J. Park and H. Ko, *Chem. Eng. J.*, 2023, **455**, 140957.
26 Q. Pan, N. Tong, N. He, Y. Liu, E. Shim, B. Pourdeyhimi and W. Gao, *ACS Appl. Mater. Interfaces*, 2018, **10**, 7927–7934.
27 N. Jishnu, S. Vineeth, A. Das, N. T. Balakrishnan, A. P. Thomas, M. Jabeen Fatima, J.-H. Ahn and R. Prasanth, *Electrospinning for advanced energy storage applications*, 2021, pp. 201–234.
28 I. Kim, B. S. Kim, S. Nam, H.-J. Lee, H. K. Chung, S. M. Cho, T. H. T. Luu, S. Hyun and C. Kang, *Materials*, 2018, **11**, 543.

29 H. Oh, D. G. Seo, T. Y. Yun, C. Y. Kim and H. C. Moon, *ACS Appl. Mater. Interfaces*, 2017, **9**, 7658–7665.
30 J. Ko, A. Surendran, B. Febriansyah and W. L. Leong, *Org. Electron.*, 2019, **71**, 199–205.
31 P. P. Sharma, V. Yadav, S. Gahlot, O. V. Lebedeva, A. N. Chesnokova, D. N. Srivastava, T. V. Raskulova and V. Kulshrestha, *J. Membr. Sci.*, 2019, **573**, 485–492.
32 A. M. Stephan, K. S. Nahm, M. A. Kulandainathan, G. Ravi and J. Wilson, *Eur. Polym. J.*, 2006, **42**, 1728–1734.
33 B. Halder, M. G. Mohamed, S.-W. Kuo and P. Elumalai, *Mater. Today Chem.*, 2024, **36**, 101926.
34 A. Kumar, T. L. Williams, C. A. Martin, A. M. Figueroa-Navedo and L. F. Deravi, *ACS Appl. Mater. Interfaces*, 2018, **10**, 43177–43183.
35 P. A. Sullivan, D. J. Wilson, M. Vallon, D. Q. Bower and L. F. Deravi, *Adv. Mater. Interfaces*, 2023, **10**, 2202463.
36 M. Z. Dzulkipli, J. Karim, A. Ahmad, N. A. Dzulkurnain, M. S. Su'ait, M. Yoshizawa-Fujita, L. Tian Khoon and N. H. Hassan, *Polymer*, 2021, **13**, 1277.
37 S. Oh, H. Jung, Y.-H. Kim, M. Kim, E. Yoo, Y. J. Choi, T.-S. Yoon and H. H. Lee, *Microelectron. Eng.*, 2013, **103**, 173–176.
38 C. Park, J. M. Kim, Y. Kim, S. Bae, M. Do, S. Im, S. Yoo and J. H. Kim, *ACS Appl. Electron. Mater.*, 2021, **3**, 4781–4792.
39 E. O. Polat, O. Balcı and C. Kocabas, *Sci. Rep.*, 2014, **4**, 6484.
40 S. Westland, C. Ripamonti and V. Cheung, *Computational colour science using MATLAB*, John Wiley & Sons, 2012.
41 C. Dinesh, *Int. J. Adv. Sci. Eng. Inf. Technol.*, 2018, **8**, 74–79.
42 M. Van Haeverbeke, M. Stock and B. De Baets, *IEEE Access*, 2022, **10**, 51363–51379.
43 S. A. Mohd Noor, C. P. Wong, M. Z. Dzulkipli, M. S. Su'ait, L. Tian Khoon and N. H. Hassan, *Solid State Phenom.*, 2021, **317**, 434–439.
44 Y. J. Jang, S. Y. Kim, Y. M. Kim, J. K. Lee and H. C. Moon, *Energy Storage Mater.*, 2021, **43**, 20–29.
45 M. Rafiee and D. Nematollahi, *Electroanalysis*, 2007, **19**, 1382–1386.
46 T. Y. Yun, X. Li, S. H. Kim and H. C. Moon, *ACS Appl. Mater. Interfaces*, 2018, **10**, 43993–43999.
47 S. Abbrent, J. Plestil, D. Hlavata, J. Lindgren, J. Tegenfeldt and Å. Wendsjö, *Polymer*, 2001, **42**, 1407–1416.
48 W. Zhang, H. Li and A. Y. Elezzabi, *Adv. Funct. Mater.*, 2022, **32**, 2108341.